Astronomy & Astrophysics

Dense gas and cold dust in the dark core B217[*]

S. Hotzel[1], J. Harju[2], D. Lemke[1], K. Mattila[2], and C. M. Walmsley[3]

[1] Max-Planck-Institut für Astronomie, Königstuhl 17, 69117 Heidelberg, Germany
[2] Observatory, PO Box 14, 00014 University of Helsinki, Finland
[3] Osservatorio Astrofisico di Arcetri, Largo E. Fermi 5, 50125 Firenze, Italy

Abstract. The Barnard object B217 was observed in the infrared and radio region. The 170 μm continuum was detected with ISOPHOT, the ammonia 1.3 cm radio lines with the Effelsberg 100 m-telescope. Mapping B217SW in $(J, K) = (1, 1)$ and $(2, 2)$ inversion lines revealed the temperature and density distribution of the gas and made it possible to investigate the dynamical state of this dense core inside B217. The ISOPHOT Serendipity Survey (ISOSS) detected the cold dust emission of B217 in all of 3 slews crossing the region. Combining ISOSS with IRAS data, we derive the core parameters of the dust from FIR emission and compare them with the NH$_3$ data, which sample the densest region of the core. This study shows the power of combining ISOSS 170 μm with IRAS/HIRES data in order to study the dust characteristics in nearby star forming regions on small spatial scales. The (170 μm/100 μm) dust colour temperature is 11 K–12 K in the dense cores and 12 K–14 K in the other regions of B217. The low dust temperatures cannot be explained by attenuation of the interstellar radiation field alone and may reflect a change in the optical properties of the dust as compared to diffuse clouds. In B217SW, molecular depletion through freeze-out onto grains is suggested by the comparison of our FIR and NH$_3$ data with previous C^{18}O observations. On the basis of our ammonia data investigation, we find in B217SW dense gas with kinetic temperatures between 9 K and 12 K, increasing outwards. Using near-infrared extinction and NH$_3$ collisional excitation calculations, the fractional ammonia abundance ($N(\mathrm{NH_3})/N(\mathrm{H_2})$) is found to be 3–5×10^{-8}, and the comparison of gas and dust observations supports this range. Knowing the ammonia abundance, we calculate the thermal, turbulent and gravitational energies of the dense core, which appears to be close to hydrostatic equilibrium. Our results are compatible with B217SW being now on the verge of collapse or in an early collapse phase.

Key words. ISM: clouds – ISM: individual objects: Barnard 217 – ISM: molecules – infrared: ISM – radio lines: ISM – surveys

1. Introduction

High-mass stars form in clusters in large molecular clouds. Isolated star formation takes place in small dense cores. These may or may not be embedded in larger clouds; their evolution can be regarded as independent of physical conditions in the rest of the cloud, and single star forming events can be studied. The stars produced in this scenario are always low-mass stars. As the number of known sites of isolated star formation is limited, while many theoretical models have been developed for this star formation mode,

it is important to investigate the known cores individually. The study of core properties is an essential ingredient of any further investigation of star formation conditions.

B217 is a dark core near the southeastern end of a large dark filament belonging to the so-called Barnard's Cloud in the central part of the Taurus molecular cloud complex (see the sketch in Gaida et al. 1984). The distance to this nearby star-forming region is 140 pc (Elias 1978). On an optical image, B217 appears as a $15' \times 10'$ (0.6 pc $\times$ 0.4 pc) sized dark core, which is well separated from the diffuse sky background (see Fig. 1). The absence of stars on the POSS-II plates (detection limit 22.5 mag) over several 10 $\square'$ sized regions across the core implies an extinction of $A_V > 5$ mag relative to the immediate surroundings.

Myers et al. (1983) detected ^{13}CO and C^{18}O, Myers & Benson (1983) detected ammonia in B217. The peak position in their NH$_3$ $(J, K) = (1, 1)$ inversion line map served as reference position for further studies with other molecules, such as CS (Zhou et al. 1989), HCN,

HNC (Harju 1989), HC$_3$N (Fuller & Myers 1993), C^{18}O, DCO$^+$/H^{13}CO$^+$ (Butner et al. 1995), CS, N$_2$H$^+$ (Lee & Myers 1999). All of these are single position observations. Mizuno et al. (1995) and Onishi et al. (1996) mapped 8 $\square^\circ$ in the Taurus complex in ^{13}CO and C^{18}O respectively. Onishi et al. (1998) presented C^{18}O ($J = 1 \rightarrow 0$) integrated line intensity maps of 40 C^{18}O cores identified in the previous survey. Their core No. 22 with 3 roughly equally strong intensity peaks coincides with B217. The nearest C^{18}O peak is $\sim 3'$ offset relative to the NH$_3$ peak.

In the optical, B217 has two brightness minima which are equally deep. The shapes of the subclumps are similar ($\sim 5' \times 3'$). We denote these clumps as B217SW and B217NE with central (J2000) positions $\alpha = 4^{\mathrm{h}}27^{\mathrm{m}}47^{\mathrm{s}}, \delta = 26°18'$ and $\alpha = 4^{\mathrm{h}}28^{\mathrm{m}}10^{\mathrm{s}}, \delta = 26°21'$. The labelling follows Goodman et al. (1993), who investigated velocity gradients of dense cores. Reinvestigating the Myers & Benson (1983) data, they found the velocity gradients in the two parts of the ammonia map to point in almost opposite directions. Even though their $(J, K) = (1, 1)$ antenna temperature map does not cover the north-eastern core completely, it shows the double core morphology. In contrast to the optical, the radio emission of B217NE is weaker and less confined than that of B217SW.

There is a Class-I (Lada & Wilking 1984; Lada 1987) young stellar object (YSO) in between the cores (IRAS 04248+2612, white triangle in Fig. 1), detected in all but the 12 μm IRAS band, with a spectrum monotonically rising towards 100 μm and a bolometric luminosity of 0.3 $L_\odot$ (Chen et al. 1995). At 2 μm, a cometary shaped nebulosity extends from the YSO 40$''$ (5000 AU) to the northwest (Tamura et al. 1991), perpendicular to the axis connecting B217NE and B217SW. Hence recent star formation in B217 coexists with two dense cores without detected YSOs. The star(s) formed so far are probably too weak to have a major impact on the dense cores and one suspects that the two dense cores will form low-mass stars themselves. Hence, B217 is of interest as a typical core forming low mass stars and B217SW is a good candidate for being a dense core just prior to star formation.

We have probed the gas in the putatively densest region – B217SW – by ammonia mapping in $(J, K) = (1, 1)$ and $(2, 2)$ inversion line transitions. This allows us to derive the kinetic temperature T_{kin}, ammonia column density $N(\mathrm{NH_3})$ and total number density n of the gas. The overall dynamical state of the core is determined by comparing kinetic and gravitational energies.

Far-infrared (FIR) emission of the dust in dense cores typically peaks beyond the 100 μm IRAS band. With ISO, extending the accessible FIR wavelength range to 240 μm, it is now possible to sample the bulk of the emitted energy. We use the ISOPHOT Serendipity Survey (ISOSS) at 170 μm and compare it with 100 μm and 60 μm IRAS/HIRES maps. We derive the dust temperature T_{dust} and the total mass M_{dust} of B217 and its dense cores. We emphasize that our FIR and Radio observations *do not* sample the same spatial volume. However, combining the

results from FIR and radio observations, we get a comprehensive picture of star formation conditions in B217.

2. Observations and data analysis

2.1. FIR data

2.1.1. ISOSS

The ISOPHOT Serendipity Survey (ISOSS) (Lemke et al. 1996) recorded the 170 μm sky brightness when the satellite was slewing between two pointed observations (details in Bogun et al. 1996). The width of the slews is $\approx 3'$ resulting in a total ISOSS sky coverage of 15%. The effective angular resolution of ISOSS (FWHM of a point source profile) is larger than the diffraction limit of 93$''$ (full width at half maximum (FWHM) of the theoretical footprint model) due to effects of the fast detector movement of up to 8$'$/s. Studying the profiles of 6 repeatedly crossed calibration sources, the effective resolution was found to be 2.19$'$ with a sample standard deviation of 0.08$'$ (Hotzel 2001). The slew-width is too small to independently determine an effective cross-scan beam profile. Assuming a circular ISOSS beam profile is however a reasonable approximation, as is demonstrated by Stickel et al. (2000). A measurement of the on-board Fine Calibration Source preceded most of the slews of the survey and all slews crossing B217. For conversion of raw detector voltage to surface brightness and removal of cosmic ray hits, the methods of Stickel et al. (2000, see their Table 1, steps 1. and 3.) were used. In contrast to their processing steps necessary for the extraction of point sources, no background was subtracted. Their routine to estimate the background was used instead to flatfield the detector. In order not to affect local changes in the gradient of the background, only one average value (per pixel) for the slew was applied. No flatfield between the slews was performed.

The accuracy of the ISOSS calibration has been checked in Appendix A.1. Summarizing, we regard a 30% photometric accuracy of ISOSS (in Taurus) as a conservative upper limit.

2.1.2. IRAS/HIRES

In order to investigate the FIR energy distribution of the dust and to derive colour temperatures, we complement ISOSS with IRAS 100 μm and 60 μm intensities. To take advantage of the full angular resolution we use HIRES processed IRAS data (Aumann et al. 1990), for which we chose default HIRES processing except for switching off baseline subtraction. The 20 iterations provided us with maps of 109$'' \times 100''$ and 77$'' \times 50''$ resolution at 100 μm and 60 μm respectively (taken from the table of effective beam sizes in the beam sample image at the site of IRAS 04248+2612). These original HIRES maps have been smoothed with non-circular 2-dim. Gauss functions of the required widths and position angles to achieve a resolution of 2.2$'$ for all FIR data.
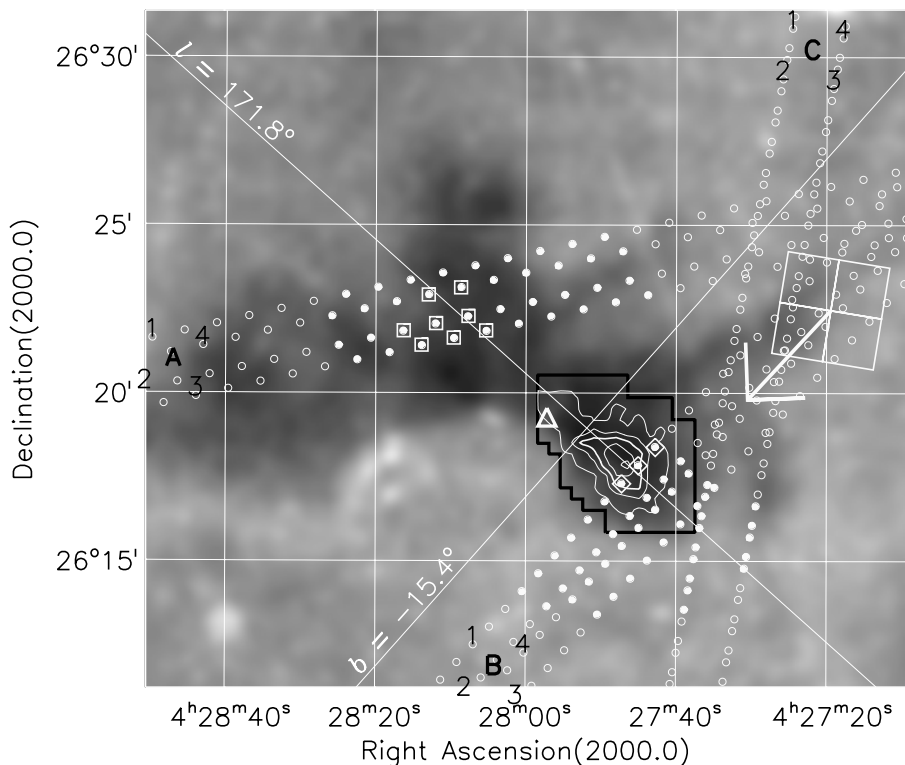
Fig. 1. B217 as dark patch on the POSS-II blue plate. After point sources had been removed, the image was smoothed to $30''$. The YSO IRAS 04248+2612 in between B217SW and B217NE is marked by a triangle. NH₃ column density contours from our Effelsberg observations of B217SW are overlayed. Figure 3 shows the same contours enlarged. Three ISOSS slews have crossed the dark core; small white circles indicate the individual pixel read-out positions. The field of view of each pixel is $90'' \times 90''$. For easier reference in this paper, we name the slews Slew A (running west to east), Slew B (west to south) and Slew C (south to north). Individual pixels are numbered. Filled circles indicate read-outs, which have been used for ananlysis of the dense cores (Fig. 8). White boxes mark positions of "anomalous" data points (Fig. 6). The detector and pixel apertures are marked on Slew B, Pixel 1&4 of which have been used in Fig. 9.

Summarizing Appendix A.2, we regard the photometric accuracy of the 100 μm HIRES map to be 30%, limited for small angular scales close to IRAS 04248+2612 by a possible ringing artefact and for the overall emission of B217 by the unknown calibration correction factor. The photometric accuracy of the 60 μm HIRES map is similar for the large scale emission. The ringing artefacts affecting investigations of the dense cores close to IRAS 04248+2612 are however much more serious, because the point source flux density is a factor 2 lower than at 100 μm, while the expected surface brightness of the cores at least a factor 10. Hence the 60 μm map is used only for a qualitative discussion regarding the FIR emission of dust in B217, but not for a quantitative estimate of temperatures (see Fig. 7).

2.1.3. Deriving dust colour temperatures

In order to derive colour temperatures and column densities of the dust, we have read out I_{100} and I_{60} intensities from the HIRES maps at all positions of the ISOSS slews in B 217 (marked in Fig. 1). The zodiacal light contribution to I_{170} has been subtracted individually from the scans, using the DIRBE model. (The offset compensation destriper in the HIRES processing has leveled different zodiacal light contributions to the individual HCONs and an additive offset does not affect our analysis.) Assuming a modified black body radiation with ν^2 emissivity,

$$I_\nu \propto \nu^2 B_\nu(T_{\rm dust}), \tag{1}$$

we can determine the dust temperature from the slope of a straight line fit to the (I_{100}, I_{170}) data points, applying

the necessary colour corrections (see also Appendix A.1.3) for the specific ISOPHOT 170 μm and IRAS 100 μm bandpasses. The underlying assumption for this procedure is that we are dealing with an optically thin source at 170 μm and 100 μm with no steep gradient in the background. Using line-fits to samples of data points, which we identify with objects on morphological grounds, we considerably decrease the scatter inherent to our FIR maps and we avoid the need to manually subtract the background from our data, which usually introduces a large bias. The accuracy of the derived colour temperature is determined by evaluating Eq. (1) for slopes multiplied by $1 + \Delta$ and $1 - \Delta$, where $\Delta = \sqrt{0.3^2 + 0.3^2 + \sigma(\text{slope})^2}$ is obtained from the ISOSS and HIRES photometric accuracies and the 1-sigma formal error of the line-fit.

If we know the FIR colour temperature and assume an isothermal cloud, we can determine the FIR opacity from the radiative transfer equation in the optically thin limit:

$$I_\nu = \tau(\nu) B_\nu(T_{\rm dust}). \tag{2}$$

In the following, the quoted values for I_ν are *not* colour corrected in order to be consistent with the figures. The correction factor ($\approx$0.92 for I_{170} and the SEDs of this paper) has been applied when converting to the physical parameters, i.e. column density and mass.

2.2. Ammonia observations

The ammonia observations were carried out in July 1988 with the Effelsberg 100 m-telescope ($40''$ beam at 23 GHz). We used a K-band maser receiver with a typical system

temperature of about 100 K on blank sky. The spectrometer used was a 1024 channel autocorrelator split into two halves with a band-width of 6.25 MHz each, centered on the frequencies of the $(J, K) = (1, 1)$ and $(2, 2)$ inversion transitions of NH_3. The velocity resolution obtained was $0.15\,\mathrm{km\,s^{-1}}$. The observations were made using position switching. The map spacing was $20''$ around the core centre and $40''$ on the outskirts of the map, the extent of which is marked in Fig. 1. The pointing was checked and the spectra were calibrated by using continuum scans towards 3C 123 for which we assumed a main-beam brightness temperature of 4.0 K. This corresponds to an observed flux density of 2.85 Jy (Ott et al. 1994), which takes into account the spatial extension ($23'' \times 5''$) of the calibration source. The pointing accuracy was found to be better than $5''$.

The hyperfine spectra were reduced using a method described by Harju et al. (1993); NH_3 fundamentals can be found in the review by Ho & Townes (1983). In a $2' \times 1.5'$ region around the peak position (see Fig. 3), the signal-to-noise ratio (SNR) in the $(1, 1)$ line was high enough to determine its excitation temperature and opacity, and the SNR in the $(2, 2)$ line was high enough to calculate the partition function. The latter is calculated assuming that only metastable ($J = K$) rotational levels are populated and the rotational temperature T_{12} (defined by $n(2, 2)/n(1, 1) = 5/3 \exp(-\Delta E_{12}/kT_{12})$) is characteristic for all metastable levels and the ground state. At positions where the optical depth could not be derived from the hyperfine spectra analysis, optically thin emission in the hyperfine groups and an excitation temperature T_{ex} (describing the relative population of the upper $(1, 1)$ state) of 10 K were assumed. $T_{12} = 10$ K was assumed at positions without a detected $(2, 2)$ transition. Using these assumptions we could trace the ammonia column density $N(NH_3)$ over almost 2 orders of magnitude. The determination of the kinetic temperature T_{kin} was restricted to the central region, where T_{ex} and T_{12} could be derived from the measurements. See Harju et al. (1993) for all equations used in this method.

Figure 2 shows the $(J, K) = (1, 1)$ spectrum at the peak position, as well as two theoretical spectra revealing the hyperfine structure of the transition.

3. Results

3.1. Gas

The results of our ammonia observations are presented in Fig. 3, where contours of NH_3 column density are overlaid on an image of kinetic temperature. T_{kin} could be derived only in the central part of the core (converted from T_{12} using the 3-rotational-levels-model of Walmsley & Ungerechts 1983, with collisional rate coefficients from Danby et al. 1988). In all positions where T_{ex} and T_{12} could be derived from the measurements we have compared $N(NH_3)$ values with column densities assuming $T_{\mathrm{ex}} = T_{12} = 10$ K (this assumption has to be used in
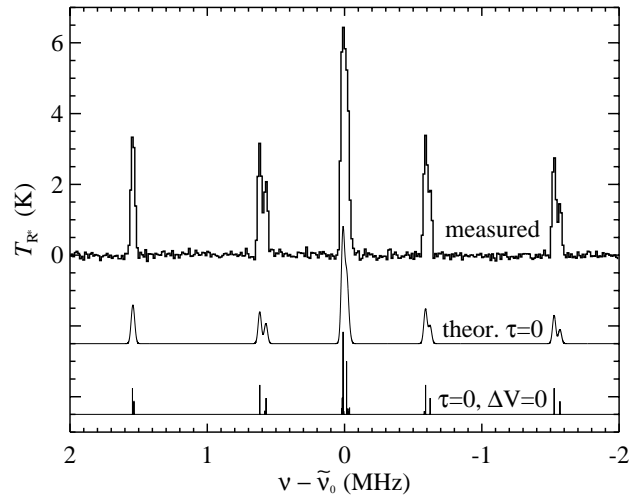
Fig. 2. Hyperfine structure of the $(J, K) = (1, 1)$ inversion transition of ammonia. The upper line is the calibrated spectrum at the peak position. The y-axis gives the antenna temperature corrected for atmospheric transmission T_{R}^*, the x-axis gives the frequency offset from the central frequency of the transition, corrected for the relative velocity of the cloud ($\tilde{\nu}_0 = 23.6945\,\mathrm{GHz} - V/c$, with $V_{\mathrm{LSR}} = 7.025\,\mathrm{km\,s^{-1}}$ at the peak position). Thin lines: Theoretical spetra for emitting gas with very low opacity ($\tau_\nu \ll 1 \Rightarrow T_{\mathrm{R}}^*(\nu) \propto \tau_\nu$). The upper theoretical curve has the same line-width as the displayed measurement. (Here $\Delta V = 0.35\,\mathrm{km\,s^{-1}}$; ΔV is the FWHM of the individual Gaussian hyperfine components and is due to thermal, turbulent and instrumental line broadening). The optical depth of the transition can be determined by evaluating the difference between this curve and the measured spectrum in the relative heights of the 5 hyperfine groups. (Here $\tau(1, 1, m) = 3.3$, where $\tau(1, 1, m)$ is the sum of the opacity peaks of the 8 hyperfine components melting together to the main group.) The bottom graph reveals the quantum mechanical transition propabilities of all 18 hyperfine components. A theoretical spectrum with vanishing opacity and line-width would assume this shape.

the outer region). Using this assumption turned out to overestimate $N(NH_3)$ by at most 60% and underestimate $N(NH_3)$ by at most 20%. Hence the detection of the $(J, K) = (1, 1)$ main group should be sufficient for a fairly reliable NH_3 column density estimate in the outer regions of B217SW. We note that inside the half maximum intensity contour of the $(1, 1)$ transition – that is where the most important cloud parameters are to be determined – no assumptions regarding T_{ex}, T_{12} or τ had to be made.

The size of B217SW is $2.3' \times 1.4'$, taking the major and minor diameter of the half maximum contour of the $(1, 1)$ line area. The geometrical mean diameter is 0.073 pc = 15 000 au. The column density contours are centred on $\alpha(2000) = 4^{\mathrm{h}}27^{\mathrm{m}}47^{\mathrm{s}}, \delta = 26°18'10''$ northeast of the actual peak position with $N(NH_3) = 1.7 \times 10^{15}\,\mathrm{cm^{-2}}$. As this offset is less than 1/2 of the diagonal step size of the map, it is possible that the offset would get smaller with higher angular resolution observations. Towards the south-east, the peak column density falls of
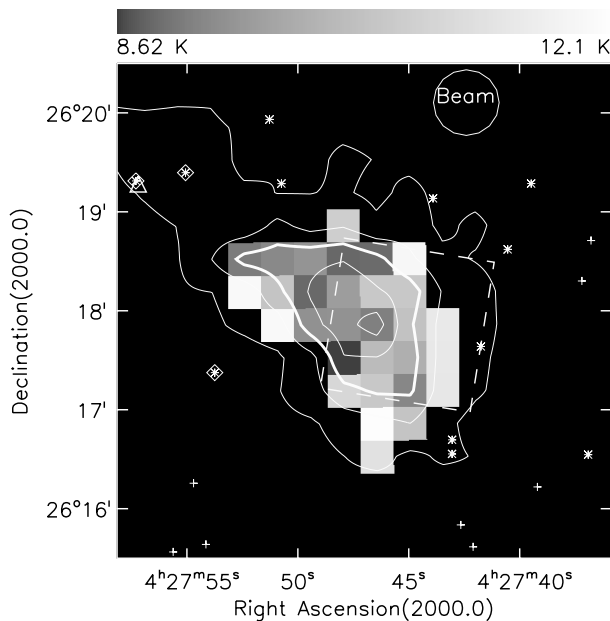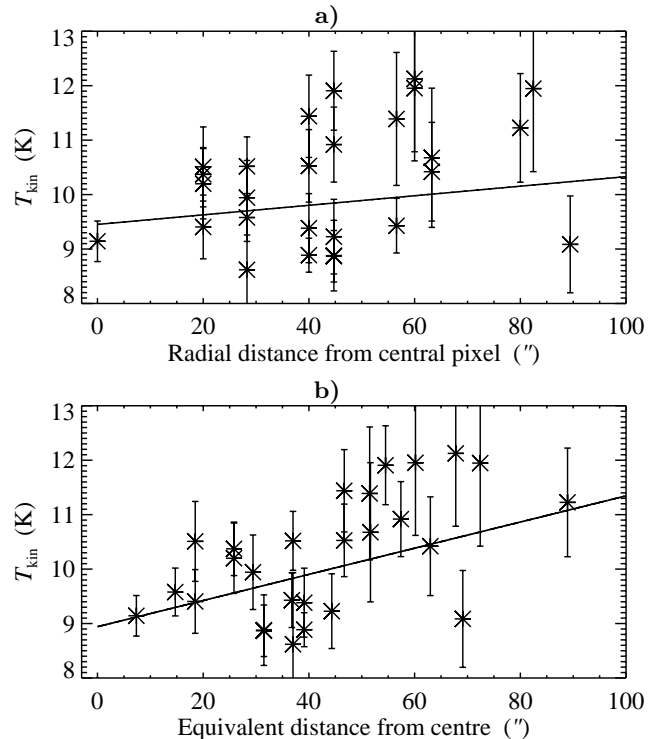
Fig. 3. Kinetic temperature (image) and NH$_3$ column density (contours) of B217SW. T_{kin} could be determined in the central part only (see text), and its range is indicated by the colour bar at top of the figure. Contours are drawn at 0.1, 0.3, 0.5, 0.7 and 0.9 × 1.7×10^{15} cm^{-2}, the peak value of N(NH$_3$). The half maximum contour is highlighted. The dashed square represents the aperture of one ISOSS detector pixel, and its position and position angle correspond to the scan read-out closest to the ammonia peak (compare Figs. 1 and 9). Plus signs and asterisks mark the positions of 2MASS point sources. Asterisks are used inside the region, where ammonia was detected and N(NH$_3$) derived. These objects were used to calculate χ(NH$_3$) except for the possibly embedded stars encased by diamonds (one of which is coincident with IRAS 04248+2612 marked by the triangle). Note that all stars used for the analysis are close to or outside the 10%-contour.

Fig. 4. Radial distribution of the kinetic temperature. Error bars are 1-sigma uncertainties. **a)** The abscissa values are the radial distances to the peak position in the NH$_3$ column density map (Fig. 1). χ^2-fitting of a radial temperature gradient reveals an outward temperature increase of 0.53 K/$''$ (solid line). **b)** Here, the abscissa values are calculated taking the aspect ratio of the dense core into account: offsets in the direction of the major and minor axes are multiplied by $(2.3/1.4)^{-1/2}$ and $(2.3/1.4)^{1/2}$ respectively. before calculating the angular distance. Additionally, it is assumed here that the true centre of the dense core is not in the centre of the map pixel, but shifted by 1/3 of a map pixel (observational step size) to the east and to the north (as suggested by the contours in Fig. 3). The fitted temperature gradient of (1.44 ± 0.43) K/$''$ corresponds to 3.5 K/0.1 pc.

by a factor of 10 in just $1'$, while the decline in the other directions is less steep.

The gas temperature is less homogeneous than found in other cores (e.g. by Lemme et al. 1996). The kinetic temperature varies by 3 K over the densest part of the core, while the typical uncertainty in T_{kin} is ~1.5 K. Despite this variation, an inside out gradient can be identified, as shown in Fig. 4. The sign of the overall temperature gradient holds to a 3-sigma level.

The number density of molecular Hydrogen n(H$_2$) can be estimated from NH$_3$ data by balancing collisional excitation against emission (Ho & Townes 1983; we used again the rate coefficients from Danby et al. 1988). This number is close to, but not equal to, the maximum density along the line of sight. The quantities T_{ex} and T_{kin} implicitly sample the source function along the line of sight, but are dominated by the region of highest density. The method fails if the density gets high enough to thermalise the (1, 1) inversion transition ($T_{ex} = T_{kin}$), which is the case in the centre of our map. Here we derive a lower limit for the

central density by using $T_{ex} - \sigma(T_{ex})$ and $T_{kin} + \sigma(T_{kin})$. Figure 5 shows the radial density profile of B217SW.

To calculate the total mass M_{NH_3} of the dense core, the abundance of ammonia relative to the dominating species H$_2$ and He has to be known. In the following we assume χ(He) = 0.2, i.e. 5 H$_2$ molecules per He atom. Various methods were applied in the past to derive the fractional ammonia abundance χ(NH$_3$) $\equiv$ N(NH$_3$)/N(H$_2$) of dense cores. Benson & Myers (1983) compared NH$_3$ with C^{18}O abundances in 10 nearby dense cores (most of them in Taurus) and found χ(NH$_3$) varying between 3 × 10^{-8} and 2 × 10^{-7}, where the N(C^{18}O) to N(H$_2$) conversion by Frerking et al. (1982) was used. Recent findings that CO is depleted in cold, dense cores (Willacy et al. 1998; Caselli et al. 1999) suggest that these values might be too high. On the other hand, C^{18}O traces also less dense regions than NH$_3$ and these two effects could partially cancel out. Taking the rounded average of this sample yields NH$_3$ = 10^{-7}. Harju et al. (1993) calculated
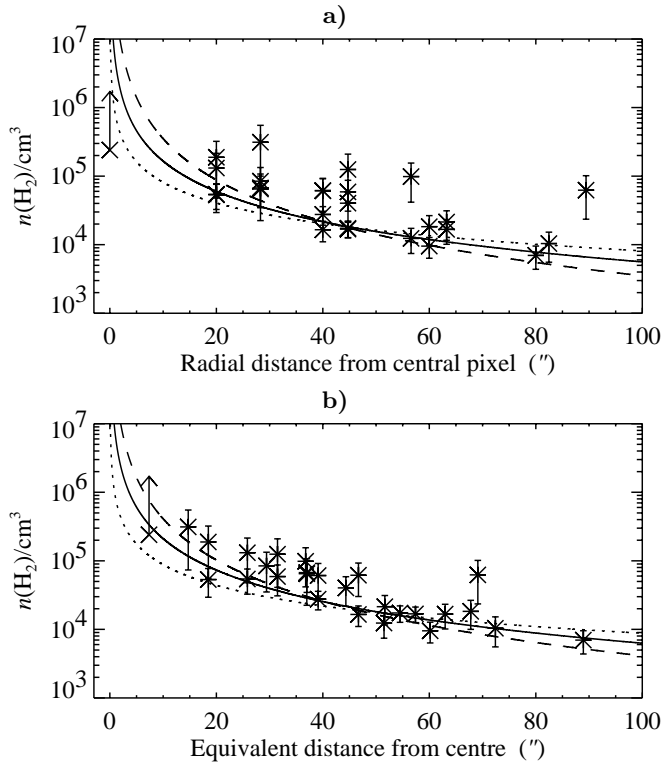
Fig. 5. Radial distribution of the H_2 number density with 1-sigma error bars. At the peak position only a lower limit can be given, indicated by an arrow at the leftmost data point (see text for details). The solid lines represent χ^2-fits of a power law ($n(r) \propto r^{-p}$). For comparison, the dotted and the dashed curves represent $n \propto r^{-1}$ and $n \propto r^{-2}$ density declines respectively. **a)** and **b)** differ in the way the angular distance is calculated (see Fig. 4). The best fitting power law exponents are $p = 1.5 \pm 0.3$ in both, **a)** and **b)**.

$\chi(NH_3) = N(NH_3)/(Ln(H_2))$ (where L denotes the assumed core size along the line of sight, taken to be twice the half-power diameter) on the basis of NH_3 data alone and found a median of 2.6×10^{-8} for 22 ammonia clumps in Orion. They obtained similar results when comparing their NH_3 column densities with ^{13}CO data. The difference in the average $\chi(NH_3)$ values of the Taurus sample (Benson & Myers 1983) and the Orion sample (Harju et al. 1993) is likely to be a systematic effect of the different methods applied and/or the different regions investigated. However, the scatter in $\chi(NH_3)$ for the Orion sources as well as for the Taurus sources is large and probably intrinsic to the sources. Therefore we have investigated B217SW itself.

First we have followed Harju et al. (1993) calculating $N(H_2) = Ln(H_2)$. Instead of using this method for statistical analysis in samples of cores we have applied it to all positions in one core and found a median $\chi(NH_3) = 4.4 \times 10^{-8}$. For comparison, we have also derived $N(H_2)$ performing a NIR reddening analysis using the point source catalogue of the Two Micron All Sky Survey (2MASS, Cutri 1997). There are 12 stars in the region of our map, where $N(NH_3)$ could be derived (see

Fig. 3). Using the method presented by Wilking et al. (1997), field stars are disentangled from possibly embedded stars (diamonds in Fig. 3) using colour-magnitude (K vs. $H - K$) and colour-colour ($J - H$ vs. $H - K$) diagrams. The remaining 9 objects have J, H and K magnitudes compatible with magnitudes of reddened low-mass dwarf or giant stars. Converting $J - K$ colours to H_2 column density we follow Lehtinen & Mattila (1996 and references therein) using $(J - K)_0 = 1.1$ mag and Harjunpää & Mattila (1996 and references therein) using $N(H_2)/E(J - K) = 5.4 \times 10^{-21}$ cm^{-2}/mag. Comparing these values with our NH_3 column densities we get $\chi(NH_3) = (2.9 \pm 1.2) \times 10^{-8}$, where the uncertainty is the sample standard deviation. On this basis, we will assume in the following $\chi(NH_3) = 4 \times 10^{-8}$ while regarding 10^{-7} and 2.6×10^{-8} as upper and lower limit respectively.

For the $2.3' \times 1.4'$ region inside the half maximum contour we derive a total mass of the core $M_{NH_3} = 2.4\ M_\odot$. Integrating further outwards down to the detection limit we find $M_{NH_3} = 4.5\ M_\odot$. The error is less than 40% if one neglects the uncertainty in $\chi(NH_3)$, which is roughly a factor 2 (see above).

To assess the dynamical state of the core, we have compared the gravitational with the kinetic energy, the latter consisting of thermal, turbulent and systematic motions. All of these four energies are calculated on the basis of our NH_3 column density map, using only pixels inside the half maximum contour. With assumptions for $\chi(He)$ and $\chi(NH_3)$ this map is converted into mass (dM) and total number of particles ($\mathcal{N}$) along each line of sight. Additionally we use maps of T_{kin} for E_{therm}, V_{lsr} for E_{syst} (which includes rotation), and $\Delta V_{turb} \equiv (\Delta V^2 - \Delta V_{inst}^2 - 8\ln 2\, kT/17m_H)^{0.5}$ for E_{turb}, where $17m_H$ is the mass of the ammonia molecule and ΔV_{inst} the instrumental line broadening, for which we take the velocity resolution of the spectrometer 0.15 km s^{-1}. For E_{pot} we must estimate the cloud thickness, which is assumed to be 0.094 pc (the major axis FWHM), over which we evenly distribute the mass along each line of sight.

We find $E_{pot} = -5.7 \times 10^{35}$ J. Relative to $|E_{pot}|$ the other energy estimates are $E_{therm} = 40\%$, $E_{turb} = 9\%$ and $E_{syst} = 4\%$, which add up to 53%. We conclude that the core is close to hydrostatic equilibrium, which requires $E_{pot} = -2E_{therm}$. As a velocity gradient of 3.7 km s^{-1} pc^{-1} in south-west to north-east direction has been detected, rotation is likely to be present, which accounts for most of the systematic motions: using Eq. (5) of Goodman et al. (1993) to calculate the ratio of rotational (E_{rot}) to gravitational energy of a core with density distribution $n \propto r^{-2}$ and given mass, radius and angular velocity (with inclination i) we find $E_{rot}/|E_{pot}| = 0.016/\sin^2 i$ (increasing for a shallower density law). Even though rotation is detected, it is unimportant for the energy balance as found in most of the known ammonia cores (Goodman et al. 1993). The low ratio of turbulent to thermal energy is however more rare and almost exclusively found in Taurus cores. Thermal motions provide most of the pressure balancing gravitation, and turbulence is hardly present.
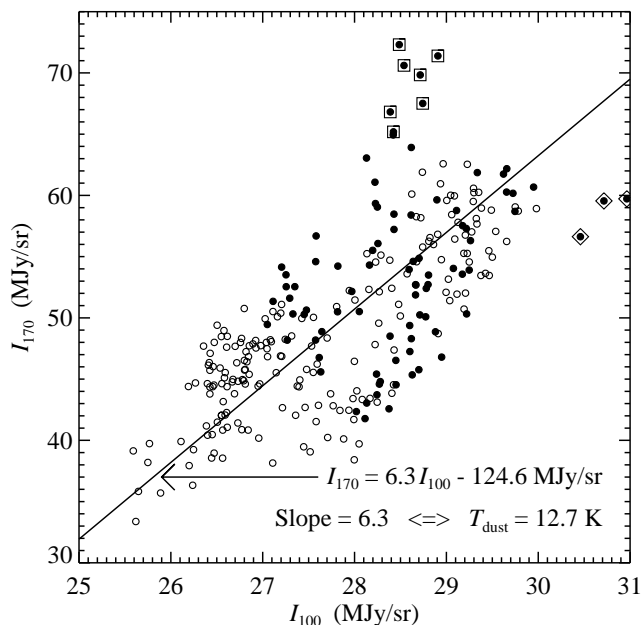
Fig. 6. I_{170} vs. I_{100} correlation plot for B217. All slew data points in the region (as displayed in Fig. 1) are used. As in Fig. 1, filled circles represent read-outs close to the two dense cores, circles encompassed by boxes represent anomalous data points. These show suspiciously high values of I_{170} (upright boxes, "□") or I_{100} (diamonds, "◇"). The solid line is fitted to all the data, its slope corresponds to an average temperature of 12.7 K. Discarding the outliers would change the fit only slightly, the FIR colour temperature would be 12.9 K.

The most crucial parameter assumed for computing the energies is the ammonia abundance $\chi(\mathrm{NH_3})$, which enters linearly in the kinetic terms but as the square in the gravitational energy. The model of the density distribution along the lines of sight is less crucial, because when calculating potential energies, the spatial distribution in 2 dimensions is taken from the map and only 1 dimension is guessed. Varying the thickness by a factor of 2 changes E_{pot} less than 25%. Neither of these two ingredients has an impact on the high ratio $E_{\mathrm{therm}}/E_{\mathrm{turb}} = 4.4$.

3.2. Dust

3.2.1. Dust temperature and opacity

The overall dust temperature of B 217 has been derived by fitting a straight line to the $I_{170} - I_{100}$ scatter plot (Fig. 6), using all data points (ISOSS and corresponding HIRES) from the 3 slews in the rectangular region displayed in Fig. 1. The slope corresponds to $T_{\mathrm{dust}} = 12.7$ K with a negligible formal error of the line-fit. Taking the uncertainty of the FIR data into account, the result is $T_{\mathrm{dust}} = (12.7^{+2.1}_{-1.1})$ K.

The comparison of FIR emission at 100 μm and 60 μm is shown in Fig. 7. No meaningful average (100 μm/60 μm) colour temperature can be assigned to B217. The lack of correlation between I_{60} and I_{100} can be understood in two ways. Firstly, artefacts due to the nearby FIR point source
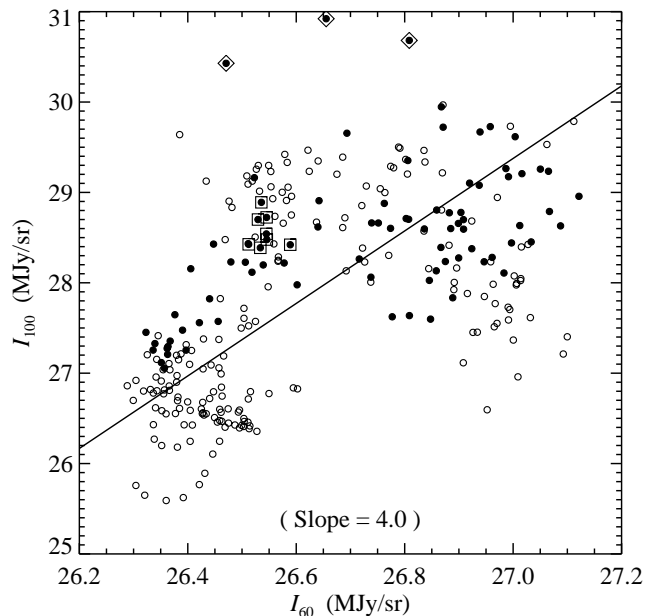

Fig. 7. I_{100} vs. I_{60} correlation plot for B217, using HIRES map read-outs at the same positions as used for Fig. 6. The anomalous data points as defined by Fig. 6 are marked using the same symbols as there. At best some sub-groups of data points show a linear correlation between 100 μm and 60 μm, but colour temperatures derived that way would be arbitrary.

(Sect. 2.1.2) may dominate any real I_{60} emission of B217. Secondly, emission from very small grains (see e.g. Désert et al. 1990) may contribute substantially to I_{60}, and this may not be spatially correlated with emission from the big grain component. This latter explanation includes emission from background/foreground structures, which could be stronger than the emission of B217 at 60 μm but not at 100 μm: if neither big grains of B217 (too cold) nor very small grains of B217 (not present) contribute to I_{60}, then one is left with background fluctuations (from standard dust components) and/or map processing artefacts. Dust coagulation in dense cores, which could be responsible for the exceptionally cold big grains (see Sect. 4), would rapidly deplete the very small grains (Ossenkopf 1993 modelling the coagulation process in dense cores with $n > 10^6$ cm^{-3}). Observational evidence of this connection is found e.g. by Bernard et al. (1999). Other dark cores without embedded FIR point sources (to exclude artefacts) need to be investigated to confirm the universality of this result.

To estimate the dust temperature of the dense cores themselves we have fitted straight lines to the data points of each of them individually (Fig. 8). For each NH$_3$ core, only read-outs within 5$'$ radius have been used (cf. Fig. 1). Due to a secondary peak in the FIR data north-west of B217SW (see below) we have excluded slew positions on that side of B217SW. Converting the slopes to colour temperatures we find $T_{\mathrm{dust}} = (12.0^{+1.9}_{-1.0})$ K in B217SW and $T_{\mathrm{dust}} = (11.1^{+1.8}_{-0.8})$ K in B217NE.

Some care must be taken because for a small number of data points an accurate I_{170} vs. I_{100} correlation
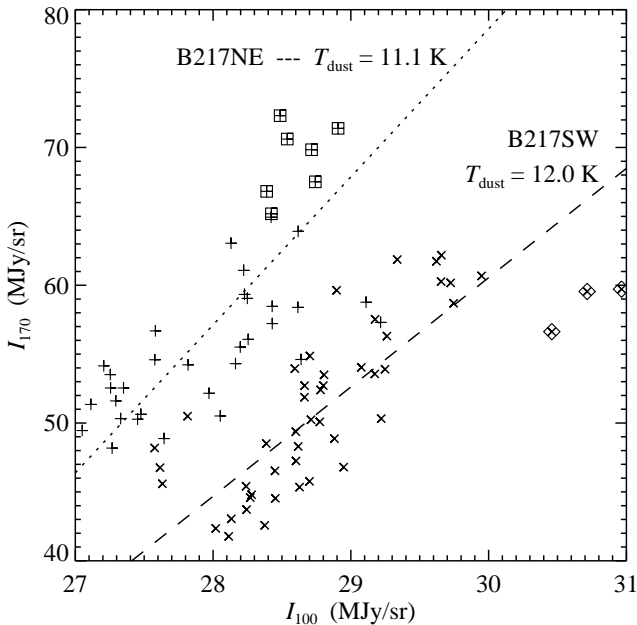
Fig. 8. I_{170} vs. I_{100} correlation plot for the two dense cores B217NE (plus signs, "+") and B217SW(crosses, "×"). Data points used in this figure are marked by filled circles in Figs. 6 and 1. For morphological reasons we used the following selection criteria: Distance <5′ from the core centres, taking the I_{170} peak position for B217NE and the NH_3 peak position for B217SW, excluding data points beyond the intensity trough (see Fig. 9). Individual fits for B217NE (dotted line) and B217SW (dashed line) correspond to colour temperatures of 11.1 K and 12.0 K respectively. Boxes represent anomalous data points as in Fig. 6. With respect to the data of the individual cores however, I_{170}-high values do not appear as outliers, but represent the general trend of B217NE. I_{100}-high values in contrast, do not match the trend of B217SW. Most likely they are due to artefacts caused by the nearby point source IRAS 04248+2612 as discussed in Appendix A.2.1. Averaging over a large sample of data points, we can cope with the uncertainty introduced by these artefacts.

is limited by (a) ISOSS flatfielding uncertainties, (b) HIRES processing artefacts due to the nearby IRAS point source. (a) is critical when using individual detector pixels, (b) is critical when using a small region only. For an estimate of the uncertainty in the derived dust temperature of the cores, we assume that structures up to 1 MJy sr^{-1} in the HIRES map can be introduced by the nearby YSO (Appendix A.2.1). As the 100 μm emission of the two cores is of the order 2 MJy sr^{-1} (offset of $I_{100} \approx 27$ MJy sr^{-1} in Fig. 8 is background) this would distort the linear correlation in Fig. 8, but it cannot be responsible for the good correlation in the first place. Particularly B217SW shows some anomalous data points, which can be explained by this artefact. It is however not justified to exclude the data points, which apparently do not fit the general trend, because *all* I_{100}-values may be affected. Instead, these effects have been taken into account with the error estimate, which is the quadratic sum of the formal line-fit error and the 43% of the FIR data (see above). In case of B217NE,

I_{100} does not exceed 29 MJy sr^{-1}, leaving some data points with suspiciously high I_{170} values. The finding that 100 μm-intensities become saturated for $A_V \gtrsim 2$ mag– 5 mag was found before in other cores (Laureijs et al. 1994; Boulanger 1994) and is the imprint of a temperature decrease in the inner regions. Consequently the derived average temperature in B217NE is slightly lower than in B217SW. However, the uncertainties discussed above do also apply here (even though artefacts are less apparent), and within the uncertainties the temperatures of B217SW and B217NE are equal. The temperatures derived this way are still averaged over ∼50 data points and therefore not too sensitive to the anomalous data points. But the artefacts on small angular scales discussed above do not allow us to trace temperature differences inside the dense cores.

There is a second I_{170}-peak only 3′ northwest of B217SW (see Fig. 9) at $\alpha(2000) = 4^h27^m33^s, \delta = 26°20′$. We are lacking any velocity information and cannot discriminate between a separate dense core, detached in space, and a secondary peak of the same core. As the ammonia clump is clearly identified with *one* of the I_{170} maxima, we regard the secondary peak as independent core and name it *B217NW*. With a FWHM of 4.4′ in north–south direction it has a similar size as B217SW. The temperature is derived in the same way as for B217SW (not included in Fig. 8 for the sake of visibility), while again no data points on the other side of the intensity valley have been used, thus allocating data points *either* to B217SW *or* to B217NW. With $T_{dust} = (13.3^{+2.4}_{-1.2})$ K, B217NW is slightly warmer than the two dense cores seen in the optical and in the ammonia maps. As the derived "average" temperature of B217 is influenced by B217NE and B217SW, the temperature of B217NW might actually be representative for the average temperature of the lower density regions of B217.

We have calculated the FIR opacity of B217SW from Slew B. After subtracting a linear baseline to exclude FIR background emission (cf. Fig. 9) we find $I_{170,max}$(B217SW) = 16 MJy sr^{-1} and $\tau(170) = 0.0025$. Converting this value to hydrogen column density we get $N(H_2) = N_H/2 = 3.6 \times 10^{21}$ cm^{-2}, where the value for the 170 μm absorption cross section per H-nuclei ($\sigma_H = 3.5 \times 10^{-25}$ cm^2) has been taken from Lehtinen et al. (1998, scaled with factor $(200/170)^2$ from their 200 μm value).

3.2.2. Flux density and dust mass

We have used different methods to estimate the total flux densities of the dark core and its dense cores. For B217SW the 1-dimensional scans (Fig. 9) were taken to model a 2-dimensional Gaussian. As Slew B is crossing the core parallel to its minor axis, the width in this direction can be accurately measured. Due to the proximity of B217NW, the Gauss function was fitted to the south easterly wing only (right hand side in Fig. 9), and a FWHM of 4.4′ was found. The actual I_{170} peak is measured by Pixel 4, passing 1.7′ southwest of the NH_3 peak. Flatfielding
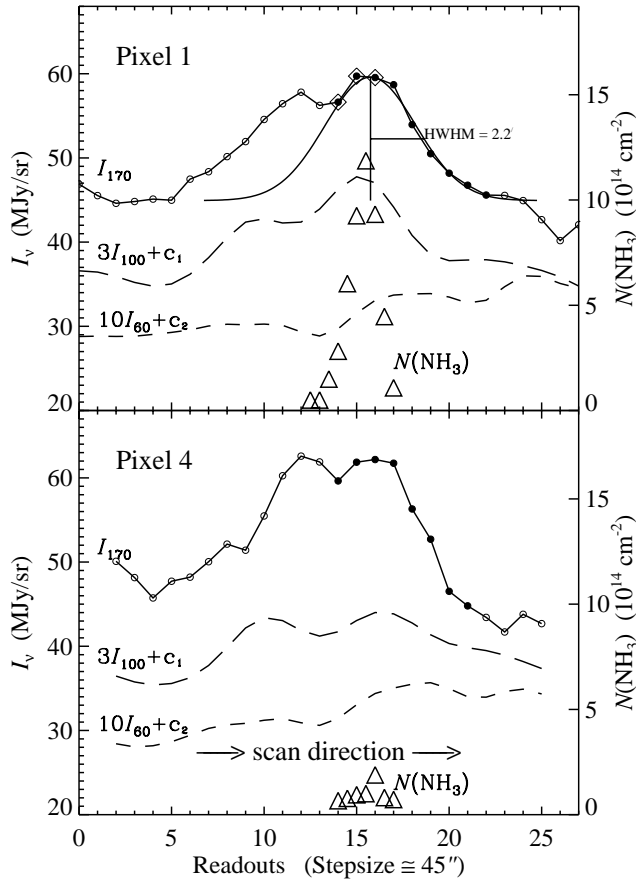
Fig. 9. Pixel 1 (upper plot) and Pixel 4 (lower plot) of Slew B crossing B217SW (see Fig. 1). The slew is crossing the ammonia core perpendicular to its major axis. Pixel 1 is crossing the core almost centrally (see Fig. 3), Pixel 4 runs $75''$ off. The plots show the profiles of I_{170} (solid line), I_{100} (long dashes), I_{60} (short dashes) and NH_3 column density (triangles). I_{100} and I_{60} are multiplied by 3 and 10 respectively (and shifted by suitable constants $c_1 = -45$ MJy sr^{-1}, $c_2 = -235$ MJy sr^{-1}) for easier comparison with I_{170}. Values for $N(NH_3)$ can be read from the right hand side y-axis. Overplotted on the I_{170}-curve are the same symbols as used in Figs. 1 and 6 in order to facilitate identification of positions. The Gauss function is used for estimating the FIR flux density (see text). Pixel 4, passing $1.7'$ off the NH_3 peak position, measures the peak intensity, but confusion with the FIR core northwest of B217SW is likely. An offset between the NH_3 peak and the FIR peak of B217SW is however possible, as the dust emission originates in a larger volume than the ammonia emission. See text and Fig. 7 for a discussion of I_{60}.

inaccuracies can also lead to 10% differences between pixels, but most likely the measured I_{170} peak is due to a projection on the north-westerly FIR core. Therefore we have used Pixel 1 for the determination of the source profile. Taking the shape to be circularly symmetric, we get $F_{170} \equiv F_\nu(170\ \mu m) = 27$ Jy.

In a second method to estimate the flux density of B217SW we have performed aperture photometry. The HIRES map (100 μm) cannot be used, because I_{100} is contaminated by the YSO point source over half of the area of B217SW and the 100 μm surface brightness is too

low to allow a reliable background subtraction. Therefore a 170 μm slew map has been created, which is incomplete, but covers B217SW to ~70% including the central position. The strong point of the slew map is to take advantage of the 2-dimensional information provided by the different pixels and slews. Taking the background to be the median of the slew map values south of B217SW, and separating emission of B217SW from the secondary peak by cutting along the valley between the two maxima (compare Fig. 9), the integrated intensity sums up to $F_{170} = 17$ Jy. This number underestimates the flux density because of the incomplete coverage at the northeast and the sharp cut at the northwest of the core. Together this may account for the 37% flux loss compared with the value from the Gaussian fitting. However, these considerations seem to exclude a value of ~50 Jy, which would result from the Gaussian method assuming the FIR axis ratio to be the same as in ammonia.

FIR emission of B217NE is more centrally peaked than that of B217SW. The FWHM is $3.4'$ in the east–west direction. The relative signals of the four pixels are in agreement with a north–south extension of $3.4'$, too. Assuming a circular shape, the flux density is 22 Jy. Pixels 2&4 show the strongest signals, i.e. the peak emission is covered by the slew. The coordinates are $\alpha = 4^h28^m08^s$, $\delta = 26°22'30''$, which is $1.5'$ north of the brightness minimum in the optical. As there is no second slew crossing, the slew map does not give any additional information. For B217NW we have used the same method as for B217SW as the half width at half maximum (HWHM) is the same in both cores. The derived flux density of B217NW is 32 Jy.

The flux density of the whole dark core B217 is difficult to derive, because the profile is not Gaussian and the coverage of the slew map is only ≈50%. The integrated flux from the slew map is $F_{170} = 95$ Jy, hence the total flux density regarding the coverage is about 200 Jy. This value can be complemented with the integrated flux at 100 μm, which is 47 Jy in a region of 280 □' (slightly larger than the dark field in Fig. 1). Subtracting the 9 Jy point source (attributing it to hot circumstellar dust) and using the derived average temperature of 12.7 K, the remaining 100 μm flux density corresponds to $F_{170} = 230$ Jy, which is in reasonable agreement with the slew map value. A factor 2 uncertainty must be assumed due to an uncertain background determination (low 100 μm surface brightness of B217 and small scale artefacts from the bright YSO). Taking the rounded average of the two methods, the total flux density of B217 is $F_{170} = (200 \pm 100)$ Jy.

The flux densities can be converted to mass, taking D and $\chi(He)$ as in Sect. 3.1 and using $\sigma_H(170)$ as for the column density. The full formula is

$$M_{FIR} = \frac{(1 + 2\chi(He))\, m_H\, D^2}{\sigma_H(170)\, K(170, T_d)\, B_{170}(T_d)} F_{170}, \qquad (3)$$

where m_H is the atomic hydrogen mass, and $K(170, T_d)$ is the colour correction factor. The dust parameters in B217 are summarised in Table 1.

Table 1. Parameters of B217 from FIR observations of the dust.

Parameter	B217	B217SW	B217NE	B217NW
Diameter (′)	15	4.4	3.4	4.4
T_{dust} (K)	12.7	12.0	11.1	13.3
$M_{FIR}{}^\star$ ($M_\odot$)	13	2.6	3.8	1.5

$\star$ Total mass using $\sigma_{H,170} = 3.5 \times 10^{-25}$ cm^2.

Table 2. Parameters of B217SW from NH$_3$ 1.3 cm radio spectroscopic and FIR continuum measurements.

Parameter	NH$_3$ inversion lines	FIR continuum
Size, not deconv.	$2.3' \times 1.4'$	$4.4' \times 4.4'$
Temperature	$T_{kin} = (9\text{--}12)$ K	$T_d = 12$ K
Peak col. dens.	$N(H_2) = 4 \times 10^{22}$ cm^{-2}	$N(H_2) = 4 \times 10^{21}$ cm^{-2}
Peak num. dens.	$n(H_2) > 2.5 \times 10^5$ cm^{-3}	
Total mass*	$M = 2.4\ M_\odot{}^{\star\star}$	$M = 2.6\ M_\odot$

$\star$ Using $\chi(NH_3) = 4 \times 10^{-8}$, $\sigma_{H,170} = 3.5 \times 10^{-25}$ cm^2 and $D = 140$ pc.
$\star\star$ 4.5 $M_\odot$ if integrating as well outside the half-max contour.

3.3. Comparison of gas and dust

The NH$_3$ core B217SW corresponds to a distinct 170 μm dust emission peak, which we have identified with B217SW for the good positional agreement. As outlined below, the difference in the intensity profiles from NH$_3$ and FIR observations meets one's expectations. It shows that the two tracers are most sensitive to different regions in the dense core, but does not conflict the overall identification. The gas and dust parameters of B217SW are summarized in Table 2.

The region of detectable dust emission is larger than the ammonia region. This is partly due to the resolution difference between our radio and FIR data but mainly to a real difference in the distributions. NH$_3$ column densities may vary strongly over relatively small distances due to chemical effects, leading to the well defined entities of dense cores. The FIR continuum on the other hand is more strongly affected by the emission of the host cloud. The bulk of the dust emission comes from a shell around the densest region, because the dust temperature is expected to decrease deep inside the core, while NH$_3$ emission remains detectable throughout the dense core as long as no NH$_3$ freeze out onto grains has set in.

The difference in the intensity profiles of $N(NH_3)$ and I_{170} as revealed in Fig. 9 is quantified in Table 2 in the order of magnitude difference of equivalent H$_2$ column densities. The effect of the resolution difference can be assessed by averaging NH$_3$ column densities in the aperture of the ISOSS detector pixel covering the ammonia peak position (see Fig. 3). The average column density is a factor of 2.1 lower than its peak value. Apart from this geometrical effect of the pixel's field of view, the flux density of a sharp column density peak as in ammonia would not entirely fall on one detector pixel ($\leq 64\%$ of the point spread function falls on one pixel; Laureijs 1999). Hence if the

dust emission at 170 μm was proportional to the *ammonia* column density, one would expect the ISOSS measured peak value to be a factor of 2–3 below the peak value from our ammonia map. Therefore, the measured order of magnitude difference in equivalent H$_2$ column densities cannot be attributed solely to observational aspects. The residual factor of 3–4 shows that the above assumption of proportionality between I_{170} and $N(NH_3)$ does not hold. Many effects such as change of grain properties or NH$_3$ over-abundance in the innermost core region could be responsible, but the most likely reason is a decreasing dust temperature in the core centre: if the dust temperature decreased by 2 K in the central 1.5′ as compared to the dense core averaged 12 K, 170 μm emission would drop by a factor of 4.

Dust and gas temperatures are almost equal in the lower density regions of the ammonia map. This is not self evident, as thermal coupling between gas and dust is not expected for $n \lesssim 10^4$ cm^{-3} (Krügel & Walmsley 1984). It is only expected in a $80'' \times 40''$ region around the central position, where densities $>10^5$ cm^{-3} have been found. The gas temperature shows an inside out gradient over the area of the core with central values around 9 K, so we expect the dust deep inside the core to be at that temperature, too. A putative temperature gradient of the dust in the same region could however not be traced with our 170 μm data, as mentioned above. Instead we have found a temperature difference between the dust of the dense cores (11 K–12 K for B217SW and B217NE) and the outer regions of B217 (13 K–14 K for B217 "average" and the FIR peak B217NW), which are only slightly colder than the widespread cold dust component in Taurus. The typical $(170\,\mu\text{m}/100\,\mu\text{m})$ colour temperature for the Taurus region is 15.8 K (14.2 K if recalibrating IRAS with the large scale emission gain factor, discussed in Appendix A.2.2), hence the whole star forming region is colder than the overall 17.5 K cirrus and typical for the 15 K "colder emission component" (Lagache et al. 1998).

Mass estimates from FIR and NH$_3$ observations are very sensitive to the parameters T_{dust} and $\chi(NH_3)$. A typical 15% uncertainty in T_{dust} (Sect. 3.2) results in 50% uncertainty in M_{FIR}. M_{NH_3} is proportional to $\chi(NH_3)^{-1}$, which is uncertain to a factor 2. Within these limits the comparison of M_{NH_3} and M_{FIR} provides a consistency check of those two parameters. As the dust emission region has about the size of our ammonia map, the mass derived by integrating all map pixels with reliable ammonia detections is appropriate for comparison with M_{FIR}. Comparing these two numbers, we have found M_{NH_3}(whole map) to be 70% larger than M_{FIR}. This difference is still consistent regarding the accuracy that could be expected. We note that the discrepancy points towards a lower dust temperature and/or a higher fractional ammonia abundance. For example, a dust temperature of 11 K (lower end of our temperature error bar) would increase M_{FIR} by 120%.

Finally we have compared the overall dust emission of B217 with the C^{18}O survey of Onishi et al. (1998). The C^{18}O intensity profile of B217 (core No. 22 in their Fig. 6a)

has 3 local maxima: one of which at $\alpha(2000) = 4^{\mathrm{h}}28^{\mathrm{m}}40^{\mathrm{s}}$, $\delta = 26°18'30''$ is $\sim 2'$ south of the path of Slew A. A second $C^{18}O$ peak at $\alpha = 4^{\mathrm{h}}28^{\mathrm{m}}08^{\mathrm{s}}$, $\delta = 26°22'10''$ coincides with B217NE. The third $C^{18}O$ peak at $\alpha = 4^{\mathrm{h}}27^{\mathrm{m}}41^{\mathrm{s}}$, $\delta = 26°19'50''$ is close to B217NW. The total mass of the $C^{18}O$ core is 21.4 $M_\odot$. Seeing that the actual peak position of the $C^{18}O$ core is not covered by the ISOSS slews this is in reasonable agreement with $M_{\mathrm{FIR}} = 13\ M_\odot$.

There is no feature in the $C^{18}O$ map at the position of the NH_3 core. Both $C^{18}O$ emission and 170 μm dust emission are good tracers of column density in regions with number density $\sim 10^3$–10^4 cm^{-3} (Onishi et al. 1996; Tóth et al. 2000), which is confirmed by the comparison in B217. One would expect both tracers to be sensitive at least to the outer regions of the NH_3 core, too. The finding that this is the case for I_{170} but not for $C^{18}O$ suggests molecular depletion. We note that due to the large area covered by ISOSS and $C^{18}O$ surveys, the I_{170}–$C^{18}O$ comparison may provide a useful tool for locating CO depleted cores.

4. Discussion

4.1. Dynamical and evolutionary state of B217SW

Our ammonia observations have revealed that B217SW is a strongly centrally condensed core with a half power radius of 0.037 pc, total mass $M_{\mathrm{NH_3}} = 2.4\ M_\odot$, central density $n_0 > 3 \times 10^5$ cm^{-3} and a density distribution $n \propto r^{-1.5}$. No significant turbulent or other non-thermal motions are present. The dense core is supported thermally and is close to hydrostatic equilibrium. Gravitational collapse may have started deep inside the core, but cannot be followed with our ammonia observations. Direct observations of infall motions are possible by studying self-absorption signatures in appropriate molecular line profiles (Zhou et al. 1993), but no such search has been done on B217SW.

The IRAS source in B217 did not prevent the formation of dense cores in its vicinity, even though the projected distance of 0.1 pc is rather small. A simple explanation is given by the observed nebulosity perpendicular to the axis connecting IRAS 04248+2612 and B217SW (see Sect. 1). If the main disruptive energy is released in a bipolar outflow, the formation of dense cores off-axis can proceed. B217 attains its smallest extent in the south-east to north-west direction close to the YSO. Also, the minor axis of B217SW, its rotational axis and (to 15°) the magnetic field lines (Goodman et al. 1992) all lie in this direction. This coincidence suggests either interaction between IRAS 04248+2612 and the core, or the overall direction of the magnetic field leaves its mark on all substructures of B217. Regarding the quiescence of the dark core (no apparent increase of T_{dust}, T_{gas} or turbulence) an interaction seems unlikely, and it is more appropriate to assume that a relatively undisturbed passing of the ambipolar diffusion phase lead to (almost) parallel formation of three dense cores with subsequent collapse of only one of them.

Alignment between core minor axes with magnetic fields does not occur in all molecular cloud cores. Onishi et al. (1996) found 70% of the $C^{18}O$ cores in Taurus to show alignment within $\pm 30°$, while Heyer (1988) found no statistically relevant alignment analysing ^{13}CO cores in the same region.

Ammonia is usually considered as a molecule characterizing later stages of chemical evolution. Myers & Benson (1983) and Suzuki et al. (1992) found NH_3 to be more abundant in older cores, where stars have already formed. Also chemical differentiation (as found in many cores e.g. by Zhou et al. 1994) can often be interpreted as a combination of density and age effects (Kuiper et al. 1996; Willacy et al. 1998). The missing peak in $C^{18}O$ column density at the position of B217SW (see core No. 22 of Onishi et al. 1996, 1998) suggests depletion of CO in the dense core studied here, too. A high ammonia abundance in B217SW is therefore consistent with an advanced chemical state, which in turn favours a slow dynamical evolution. This is indeed believable, as the core seems to be near hydrostatic equilibrium, and for the geometrical arguments mentioned above.

4.2. Dust properties

The dust temperature in B217 is lower than in the majority of dark cores or globules, where temperatures of 13 K–15 K prevail (Lehtinen et al. 1998; Hotzel et al. 2000). Dust temperatures of 11 K–14 K as in B217 are rare. Two dark cores with similar temperatures are B361 (11 K–13 K, Keene et al. 1983) and L183 (12 K–13 K Lehtinen et al. 2000).

Bernard et al. (1992) modelled IR emission of externally heated dust clouds and predict a $(400\,\mu\mathrm{m}/241\,\mu\mathrm{m})$ colour temperature of 15.9 K in a cloud similar in mass and density structure to B217/B217SW (their model with code 324: $n_{\mathrm{central}} = 10^5$ cm^{-3}, $n \propto r^{-2}$, $A_{V,\mathrm{central}} = 10$ mag, $M = 5.99\ M_\odot$). This is inconsistent with our results. The radiative transfer modelling can be reconciled with our observations, if dust properties in dense and cold environments differ from the adopted (Désert et al. 1990) ISM dust model. Two mechanisms could be involved. Firstly, ice mantles of molecules such as H_2O and CO freeze out onto dust grains at densities of a few times 10^4 cm^{-3} (van Dishoeck & Blake 1998), which will change the absorption properties of the grains. Secondly, coagulation of (ice coated) dust grains shifts the size distribution towards larger diameters. The "steady-state" temperature of $0.3\,\mu$m grains is $\approx$10% lower than that of comparable $0.1\,\mu$m grains (Draine & Lee 1984). The production of "fluffy" agglomerates (Mathis & Whiffen 1989) may also affect the albedo and the emissivity of the dust. Lehtinen et al. (1998) found the Thumbprint Nebula to be colder than predicted by the numerical calculations and already suggested grain growth to be responsible for the discrepancy. Bernard et al. (1999) discussed low dust temperatures in the cloud MCLD123.5+24.9, showing

that neither ISRF intensity variations nor extinction could explain the FIR/Sub-mm SED (based on IRAS, ISOPHOT and PRONAOS data) and proposed coagulation of smaller dust particles on large size grains to be responsible.

5. Conclusions

B217 is a dark core containing one Class-I YSO and two dense ammonia cores. Our ammonia observations with the Effelsberg 100 m-telescope have revealed the density and temperature distributions of B217SW. The dense core is supported by thermal pressure only and is approximately in hydrostatic equilibrium. Its minor axis, its rotational axis and the magnetic field lines are aligned and perpendicular to the axis connecting B217SW with the YSO and B217NE. This coincidence, the low degree of turbulence and the high abundance of NH_3, all point to a slow dynamical evolution, suggesting that the formation of dense cores in B217 has been governed by ambipolar diffusion. The geometrical configuration suggests that the YSO will not prevent the possible collapse of B217SW despite the slow diffusion process.

The advanced evolutionary stage of B217 is further supported by our dust observations with ISOSS. The colour temperatures of 11 K–12 K in the dense cores cannot be modeled with the same dust composition as in diffuse clouds, but can be explained by a change in dust properties due to agglomeration of dust grains. The lack of detectable 60 μm emission from very small grains in B217 provides further support for this interpretation. While there is a close correlation between $C^{18}O$ emission and I_{170} over much of the B217 area, a strong $C^{18}O$ deficiency relative to I_{170} marks the position of the NH_3 core, providing direct evidence for CO freeze out onto dust grains in B217SW.

Masses derived from the dust and the gas emission agree reasonably well and are consistent with a fractional ammonia abundance of 3–5 $\times 10^{-8}$. Temperature gradients are found for both T_{gas} and T_{dust}, which are not likely to be directly linked. However, the ranges are similar with T_{gas} between 9 K and 12 K inside B217SW, and T_{dust} between 11 K and 14 K as in B217NE and the lower density regions of B217 respectively.

We have attempted for the first time to correlate ISOSS 170 μm with IRAS/HIRES data. This has proven to be a useful method of studying dust parameters inside a low mass star forming dark core. As 14% of the sky are covered in both surveys, this may be a useful new tool to characterize the dust in a large number of clouds and cloud cores.

Appendix A: Calibration accuracies of the FIR data

A.1. ISOSS calibration

A.1.1. Positional accuracy

Stickel et al. (2000) investigated the agreement between ISOSS and IRAS positions for a large number of galaxies and found offsets $<45''$ for more than 90% of their sources. In a more recent investigation of the positional accuracy of the ISOSS slews, 2% of the slews have been identified as having uncertain positional information. In these cases, a delayed finding of the guide star of the subsequent pointed observation was likely to reduce the accuracy of the gyro drift correction, which is necessary to apply to the slew data. Using unflagged slews only, the inspection of 61 detections of Neptune, Uranus and the brighter asteroids yielded no positional offset perpendicular to the slewing direction (which can be measured more accurately), implying an accuracy of $\sim15''$ (Müller et al. 2001). The positional accuracy parallel to the slew is probably worse, because transient effects of the detector play a role. We did not try any correction for this effect because a high in-scan precision (to better than $45''$) is not crucial for our analysis.

A.1.2. Photometric accuracy

The photometric accuracy was checked by Tóth et al. (2000) comparing ISOSS results with dedicated pointed raster maps (mode AOT PHT22), which turned out to agree within $\pm20\%$ in surface brightness. The uncertainty in the absolute photometry of the mapping mode itself is again 20% (Klaas et al. 1998). Hence the photometric accuracy of an *individual* data point is 30% in case of extended emission.

The uncertainty originates partially in changing detector response, from slew to slew, within the slew and from pixel to pixel. We have estimated these effects by comparing intensities at all positions covered by more than one slew in a $16° \times 16°$ region centred on B217. We have calculated the relative brightness deviations of measurement pairs (deviation from their mean) and find a root mean square deviation of only 7.9%. (*Measurement pairs* come from different slews and have positional offsets $<30''$ between individual pixel positions.) The local accuracy of the flatfield has been checked for Slew C (Fig. 1), where every second pixel runs along the same line. The relative brightness deviations of Pixel 1&2 are 4.5%, of Pixel 3&4 are 5.8% (averaged over a scan length of $1°$).

A.1.3. Comparison with DIRBE

We will compare our ISOSS 170 μm intensities with IRAS 100 μm and 60 μm data and have therefore checked in a consistent manner the calibration of both ISOSS and IRAS. As a common reference standard, we have used the COBE/DIRBE data base (Hauser et al. 1991). As there

is no DIRBE 170 μm band, we have interpolated from the 100 μm, 140 μm and 240 μm bands by fitting a modified blackbody spectrum with a ν^2 emissivity law. For this, Eq. (1) has been used iteratively, in order to apply the necessary colour corrections. Colour corrections are necessary for all FIR data, in order to convert the quoted intensities (for which an intrinsic spectrum $I_\nu \propto \nu^{-1}$ is assumed by convention), to the real values at the reference wavelength. After interpolation, the new DIRBE 170 μm intensities have been transformed to the ISOSS filter-band (inverse colour corrections), so that I_{170}^{DIRBE} and I_{170}^{ISOSS} can be directly compared.

The result is shown in Fig. A.1a, where the $16° \times 16°$ Taurus region has been evaluated. All ISOSS values corresponding to the same DIRBE map pixel ($\approx 20' \times 20'$) are averaged. All DIRBE pixels crossed by one or more ISOSS slews are included, i.e. also a lot of uncompletely covered pixels (coverage <20% if crossed by 1 slew only). This (and the fact that the DIRBE beam has twice the pixel size) introduces some scatter, but statistically does not affect this analysis. Fitting a straight line to the data points using the ordinary least-squares bisector (OLSB) method (which treats x and y values equivalently, see Isobe et al. 1990) we derive the relation $I_{170}^{\mathrm{ISOSS}} = 1.01 I_{170}^{\mathrm{DIRBE}} + 0.1$ MJy sr^{-1} with 1-sigma errors 0.013 (gain) and 0.52 MJy sr^{-1} (offset).

A.2. IRAS/HIRES calibration

#### A.2.1. Photometric accuracy of low surface brightness features

Photometric calibration of the HIRES maps has been checked for the two FIR point sources in the field (see Fig. A.2). Aperture photometry from the maps yields 5% and 15% higher flux densities compared with the IRAS point source catalog (PSC2) for IRAS 04248+2612 and IRAS 04240+2559 respectively. This small offset can be attributed to background structures, hence HIRES processing did not change the total flux of point sources. However, the "ringing" around point sources (see e.g. Cao et al. 1997) affects our analysis of low surface brightness features near IRAS 04248+2612. Therefore we are limited to features $\gtrsim 1$ Jy (~ 1 MJy sr^{-1} over 10 $\Box'$), assuming that 10% of the YSO flux density (9 Jy at 100 μm) is contained in the ring. If the paths of the ISOSS slews cross this ring (worst case) we expect I_{100}-artefacts of at most 1 MJy sr^{-1} for the cores B217SW and B217NE. The contribution of the point source to I_{100} due to the FWHM of 2.2$'$ is smaller. The closest approach of a scan to the YSO is 2.9$'$ (Pixel 3, Slew A). A 9 Jy point source at this distance contributes with 0.16 MJy sr^{-1}. If the FWHM of the map was underestimated by 10%, the contribution is 0.30 MJy sr^{-1}.
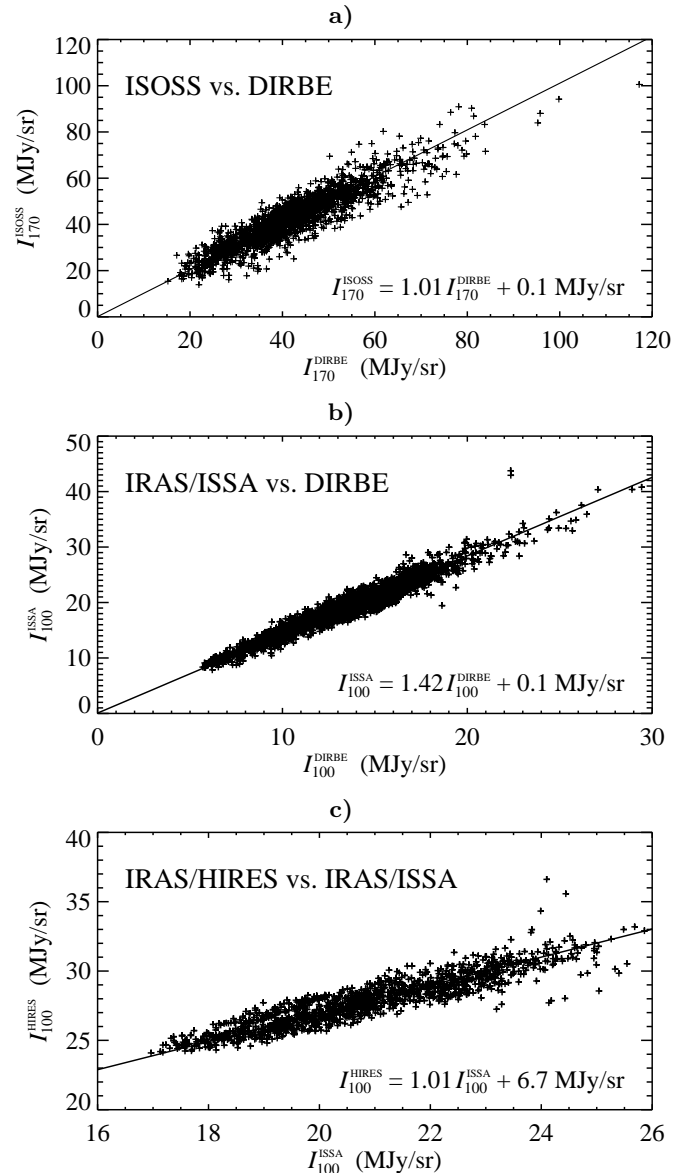
Fig. A.1. Calibration comparison of the FIR data. As the combination of ISOSS with HIRES is a novelty, we check their calibrations against DIRBE. **a)** ISOSS vs. DIRBE in the $16° \times 16°$ Taurus region. ISOSS densities are averaged in each DIRBE pixel. **b)** ISSA vs. DIRBE in the same region as **a)**; again, one data point per DIRBE pixel. **c)** HIRES vs. ISSA in the B217 area; one data point per ISSA pixel. The maps used are displayed in Fig. A.2. There is a systematic difference between IRAS and DIRBE intensities on these large angular scales, while the calibrations of ISOSS and DIRBE agree. We do *not* rescale the HIRES data used in this paper, because the gain value for very small angular scales could be different. However, as our investigated structures of sizes 2$'$–15$'$ clearly exceed the size of point sources (for the IRAS detector), the derived colour temperatures may be systematically too high (I_{170}/I_{100} too low).

A.2.2. IRAS/HIRES versus DIRBE

As we have done with the ISOSS data, we have checked the IRAS calibration against DIRBE. The HIRES maps
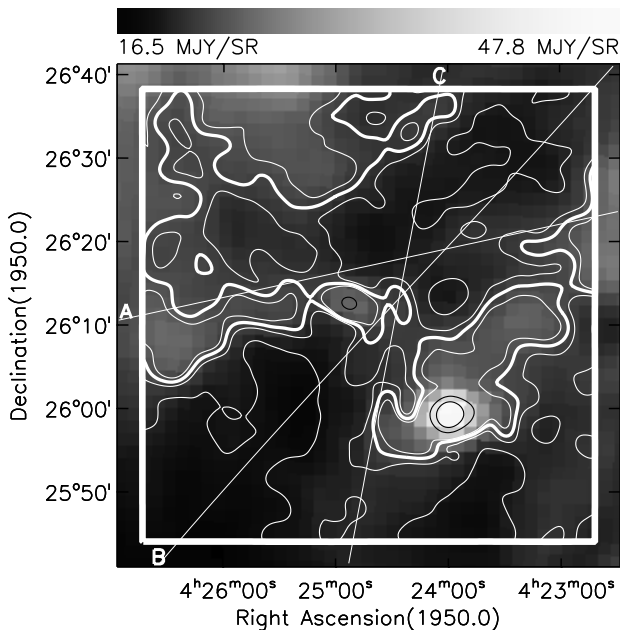
Fig. A.2. The HIRES 100 μm map (contours) used for comparison with ISOSS (i.e. smoothed to 2.2$'$) overlayed on the ISSA 100 μm map (image), which has been used to check the HIRES calibration in Fig. A.1c. The grey-scale used is indicated at the top of the figure; contours are drawn at 26, 28, 29(thick), 30, 40(black) and 60(black) MJy sr^{-1}. The white contours are chosen in order to identify the structure seen in Fig. 9, the black contours are chosen in order to mark the two bright point sources in the field. The fainter one is IRAS 04248+2612 in the centre of B217. The paths of the 3 slews crossing the dark core are overlayed (labeled "A", "B", "C").

are too small to be directly compared, therefore we have used a 2-step procedure comparing first DIRBE with the IRAS/ISSA maps (Wheelock et al. 1994) and subsequently IRAS/ISSA with IRAS/HIRES. The former step is performed in the same 16$°$ × 16$°$ region used above for the ISOSS–DIRBE comparison, and the result is shown in Fig. A.1b. All ISSA pixels falling in the same DIRBE pixel are averaged. The OLSB fit yields $I_{100}^{\mathrm{ISSA}} = 1.42 I_{100}^{\mathrm{DIRBE}} + 0.1$ MJy sr^{-1} with 1-sigma errors 0.012 (gain) and 0.15 MJy sr^{-1} (offset). This ISSA–DIRBE relation in Taurus is equal (within 1-sigma) to the all-sky relation found by Wheelock et al. (1994). Performing the same comparison for the 60 μm data we have found $I_{60}^{\mathrm{ISSA}} = 1.34 I_{60}^{\mathrm{DIRBE}} - 1.7$ MJy sr^{-1}, while the gain derived by Wheelock et al. (1994) is 1.15 ± 0.07. It is not surprising that the gain between the 60 μm data sets is less homogenous across the sky than the gain between the 100 μm data sets, because heterogenous dust populations and environments contribute to I_{60} (big grains/very small grains, interstellar/circumstellar/interplanetary dust), while I_{100} is dominated by big grains of the interstellar dust. For example, the Taurus region is close to the ecliptic, and the zodiacal light was subtracted using diffent models for IRAS and DIRBE.

The HIRES–ISSA comparison is shown in Fig. A.1c for the 1$\square°$region of the HIRES map (shown in Fig. A.2).

The HIRES pixels falling in the same ISSA pixel are averaged, but no further convolution has been performed, hence the two bright point sources in the field introduce some artificial structure. Ignoring the brightest 2% of the data points, the gain is unity, as expected. For our calibration purposes we can ignore the offset, which is due to zodiacal light that has been subtracted from the ISSA but not from the raw scan data used for the HIRES maps.

Considering the findings of Fig. A.1, I_{100} HIRES values from extended objects must be devided by 1.42 (I_{60} by 1.34) in order to be consistent with the ISOSS calibration. This correction must however not be applied to point sources, as emphasized by Wheelock et al. (1994, p. IV-16). For angular scales of the order 2$'$–15$'$, the correction factor is not known and may even change between its extremes 1 (no correction for structures as the dense cores) and 1.4 (for B217 as a whole). For this difficulty, we have not applied any correction to the HIRES data, bearing in mind that the I_{170}/I_{100} ratios needed for deriving colour temperatures could be systematically too low.

References

Aumann, H. H., Fowler, J. W., & Melnyk, M. 1990, AJ, 99, 1674

Benson, P. J., & Myers, P. C. 1983, ApJ, 270, 589

Bernard, J. P., Boulanger, F., Désert, F. X., et al. 1992, A&A, 263, 258

Bernard, J. P., Abergel, A., Ristorcelli, I., et al. 1999, A&A, 347, 640

Bogun, S., Lemke, D., Klaas, U., et al. 1996, A&A, 315, L71

Boulanger, F. 1994, Dust and Gas in the Infrared Cirrus, in The First Symposium on the Infrared Cirrus and Diffuse Interstellar Clouds, ed. R. M. Cutri, & W. B. Latter, ASP Conf. Ser., 58, 101

Butner, H. M., Lada, E. A., & Loren, R. B. 1995, ApJ, 448, 207

Cao, Y., Terebey, S., Prince, T. A., et al. 1997, ApJS, 111, 387

Caselli, P., Walmsley, C. M., Tafalla, M., et al. 1999, ApJ, 523, L165

Chen, H., Myers, P. C., Ladd, E. F., et al. 1995, ApJ, 445, 377

Cutri, R. M. 1997, The 2MASS Point Source Processing Pipeline, Design and Prototype Results, in The Impact of Large Scale Near-IR Sky Surveys, ed. F. Garzon, N. Epchtein, & A. Omont, ASSL, 210, 187

Danby, G., Flower, D. R., Valiron, P., et al. 1988, MNRAS, 235, 229

Désert, F. X., Boulanger, F., & Puget, J. L. 1990, A&A, 237, 215

Draine, B. T., & Lee, H. M. 1984, ApJ, 285, 89

Elias, J. H. 1978, ApJ, 224, 857

Frerking, M. A., Langer, W. D., & Wilson, R. W. 1982, ApJ, 262, 590

Fuller, G. A., & Myers, P. C. 1993, ApJ, 418, 273

Gaida, M., Ungerechts, H., & Winnewisser, G. 1984, A&A, 137, 17

Goodman, A. A., Jones, T. J., Lada, E. A., et al. 1992, ApJ, 399, 108

Goodman, A. A., Benson, P. J., Fuller, G. A., et al. 1993, ApJ, 406, 528

Harju, J. 1989, A&A, 219, 293

Harju, J., Walmsley, C. M., & Wouterloot, J. G. A. 1993, A&AS, 98, 51

Harjunpää, P., & Mattila, K. 1996, A&A, 305, 920

Hauser, M. G., Kelsall, T., Moseley, S. H. J., et al. 1991, The Diffuse Infrared Background – COBE and Other Observations, in After the first three minutes, ed. S. S. Holt, C. L. Bennett, & V. Trimble, AIP Conf. Proc. 222, 161

Heyer, M. H. 1988, ApJ, 324, 311

Ho, P. T. P., & Townes, C. H. 1983, ARA&A, 21, 239

Hotzel, S. 2001, Die 170-μm-Zufallsdurchmusterung mit ISO – Strukturen im kalten Staub der Milchstraße, Ph.D. Thesis, Ruprecht-Karls-Universität Heidelberg, in preparation

Hotzel, S., Lemke, D., Krause, O., et al. 2000, Chamaeleon's Cold Cloud Cores, in Proc. Workshop: ISO Surveys of a Dusty Universe, ed. D. Lemke, M. Stickel, & K. Wilke (Springer), 259

Isobe, T., Feigelson, E. D., Akritas, M. G., et al. 1990, ApJ, 364, 104

Keene, J., Davidson, J. A., Harper, D. A., et al. 1983, ApJ, 274, L43

Klaas, U., Laureijs, R. J., Radovich, M., et al. 1998, ISOPHOT Calibration Accuracies, SAI/98-092/Dc Version 2, ESA

Krügel, E., & Walmsley, C. M. 1984, A&A, 130, 5

Kuiper, T. B. H., Langer, W. D., & Velusamy, T. 1996, ApJ, 468, 761

Lada, C. J. 1987, Star formation – From OB associations to protostars, in Star Forming Regions, ed. M. Peimpert, & J. Jugaku, IAU Symp., 115, 1

Lada, C. J., & Wilking, B. A. 1984, ApJ, 287, 610

Lagache, G., Abergel, A., Boulanger, F., et al. 1998, A&A, 333, 709

Laureijs, R. J. 1999, Point spread function fractions related to the ISOPHOT C100 and C200 arrays, Tech. Rep. Version 1.0, ISO Data Centre, ESA

Laureijs, R. J., Helou, G., & Clark, F. O. 1994, The 100 Micron Emission of Clouds, in The First Symposium on the Infrared Cirrus and Diffuse Interstellar Clouds, ed. R. M. Cutri, & W. B. Latter, ASP Conf. Ser., 58, 133

Lee, C. W., & Myers, P. C. 1999, ApJS, 123, 233

Lehtinen, K., & Mattila, K. 1996, A&A, 309, 570

Lehtinen, K., Lemke, D., Mattila, K., et al. 1998, A&A, 333, 702

Lehtinen, K., Mattila, K., Lemke, D., et al. 2000, ISOPHOT Far-Infrared Survey of Nearby Molecular Clouds, in Proc. Workshop: ISO Surveys of a Dusty Universe, ed. D. Lemke, M. Stickel, & K. Wilke (Springer), 317

Lemke, D., Klaas, U., Abolins, J., et al. 1996, A&A, 315, L64

Lemme, C., Wilson, T. L., Tieftrunk, A. R., et al. 1996, A&A, 312, 585

Mathis, J. S., & Whiffen, G. 1989, ApJ, 341, 808

Mizuno, A., Onishi, T., Yonekura, Y., et al. 1995, ApJ, 445, L161

Müller, T. G., Hotzel, S., & Stickel, M. 2001, A&A, in preparation

Myers, P. C., & Benson, P. J. 1983, ApJ, 266, 309

Myers, P. C., Linke, R. A., & Benson, P. J. 1983, ApJ, 264, 517

Onishi, T., Mizuno, A., Kawamura, A., et al. 1996, ApJ, 465, 815

Onishi, T., Mizuno, A., Kawamura, A., et al. 1998, ApJ, 502, 296

Ossenkopf, V. 1993, A&A, 280, 617

Ott, M., Witzel, A., Quirrenbach, A., et al. 1994, A&A, 284, 331

Stickel, M., Lemke, D., Klaas, U., et al. 2000, A&A, 359, 865

Suzuki, H., Yamamoto, S., Ohishi, M., et al. 1992, ApJ, 392, 551

Tamura, M., Gatley, I., Waller, W., et al. 1991, ApJ, 374, L25

Tóth, L. V., Hotzel, S., Krause, O., et al. 2000, A&A, 364, 769

van Dishoeck, E. F., & Blake, G. A. 1998, ARA&A, 36, 317

Walmsley, C. M., & Ungerechts, H. 1983, A&A, 122, 164

Wheelock, S. L., Gautier, T. N., Chillemi, J., et al. 1994, IRAS sky survey atlas: Explanatory supplement, JPL Publikation 94-11, IPAC, JPL

Wilking, B. A., McCaughrean, M. J., Burton, M. G., et al. 1997, AJ, 114, 2029

Willacy, K., Langer, W. D., & Velusamy, T. 1998, ApJ, 507, L171

Zhou, S., Wu, Y., Evans, N. J., et al. 1989, ApJ, 346, 168

Zhou, S., Evans, N. J., Koempe, C., et al. 1993, ApJ, 404, 232

Zhou, S., Evans, N. J., Wang, Y., et al. 1994, ApJ, 433, 131